CrossMark

The effects of quenching on electrical properties, and leakage behaviors of $0.67BiFeO_3$–$0.33BaTiO_3$ solid solutions

Yanfeng Qin[1,2] · Jie Yang[1] · Pan Xiong[1,2] · Wenjuan Huang[1,2] · Jiyue Song[1,2] · Lihua Yin[1] · Peng Tong[1] · Xuebin Zhu[1] · Yuping Sun[1,3,4]

Abstract

Ferroelectric solid solutions of $0.67BiFeO_3$–$0.33BaTiO_3$ were prepared by a Pechini method followed by quenching process. The XRD results indicate that both the furnace-cooled and water-quenched samples are consist of rhombohedral and tetragonal phases. SEM images show that the quenching process does not change the microstructure of $0.67BiFeO_3$–$0.33BaTiO_3$ solid solutions. The quenched sample exhibits well-defined P–E hysteresis loop with remnant polarization of 23 µC/cm^2 at room temperature. The leakage mechanism of the furnace-cooled sample is Ohmic conduction mechanism, whereas the leakage mechanism of water-quenched sample is predominated by field-assisted ionic conduction at room-temperature and 50 °C and then changes to three different conduction mechanisms at 100 °C.

1 Introduction

$BiFeO_3$ is one of the most promising room-temperature (RT) multiferroic materials which has high ferroelectric Curie temperature (T_C ~ 830 °C) and antiferromagnetic Néel temperature (T_N ~ 340 °C) [1–4]. However, the pure bulk $BiFeO_3$ is difficult to prepare due to the formation of impurity phase and the thermodynamic stability of $BiFeO_3$ [5, 6]. Moreover, the relatively high leakage-current density is often observed in the $BiFeO_3$ ceramic due to the volatilization of Bi during the sintering process. The formation of oxygen vacancies and the valence variation in Fe ions (Fe^{3+} to Fe^{2+}) make it difficult to obtain the intrinsic, well-saturated polarization vs. the electric field (P–E) hysteresis loop [7, 8].

$BiFeO_3$ solid solutions such as $BiFeO_3$–$BaTiO_3$, $0.9BiFeO_3$–$0.1PbTiO_3$, $BiFeO_3$–$Na_{0.5}Bi_{0.5}TiO_3$ have attracted considerable attention in recent years owing to their excellent electrical properties and their possible application [9–13]. Among these materials, a high remnant polarization (P_r), high T_C and relatively good piezoelectric coefficient (d_{33}) can be obtained in $(1-x)BiFeO_3$–$xBaTiO_3$ with $x = 0.33$ [14, 15]. In addition, Wei et al. reported that Mn-doping can effectively improve the P_r and d_{33} of $0.7BiFeO_3$–$0.3BaTiO_3$ [16]. Thermal quenching is often used to enhance the electrical properties of $BiFeO_3$-based solid solutions. The formation of Fe^{2+} and oxygen deficiencies can be effectively suppressed by quenching $BiFeO_3$ ceramics above ferroelectric temperature [17]. The d_{33} value of $0.67BiFeO_3$–$0.33BaTiO_3$ is less than 200 pC/N for the furnace-cooled sample, whereas the d_{33} value can increase to 240 pC/N by using a water-quenching process [15, 18]. Kim et al. have studied the relations between the distribution of defect states and electrical properties of $0.8BiFeO_3$–$0.2BaTiO_3$ ceramic under different thermal treatments [19]. In addition, the structural evolution of the quenched $BiFeO_3$–$BaTiO_3$ solid solutions have been studied [20]. But there are few studies about leakage mechanisms in $BiFeO_3$–$BaTiO_3$ solid solutions under different thermal treatments. The leakage property is a critical characteristic in practical applications of ferroelectric materials. Moreover, it is closely related to the ferroelectric performance and the thermal stability of electronic devices [21, 22]. Therefore, It

✉ Jie Yang
  jyang@issp.ac.cn

[1] Key Laboratory of Materials Physics, Institute of Solid State Physics, Chinese Academy of Sciences, Hefei 230031, People's Republic of China

[2] University of Science and Technology of China, Hefei 230026, People's Republic of China

[3] High Magnetic Field Laboratory, Chinese Academy of Sciences, Hefei 230031, People's Republic of China

[4] Collaborative Innovation Center of Advanced Microstructures, Nanjing University, Nanjing 210093, People's Republic of China

is necessary to investigate the electrical properties and leakage mechanisms of $BiFeO_3$–$BaTiO_3$ solid solutions.

In this manuscript, we prepared the $0.67BiFeO_3$–$0.33BaTiO_3$ (67BF–33BT) solid solutions by a Pechini method followed by a quenching process. We investigated the electrical properties and leakage mechanisms of 67BF–33BT solid solutions with different thermal treatments at different temperatures.

2 Experimental details

Polycrystalline 67BF–33BT ceramics were synthesized via a Pechini method. We added 5% excess of Bi to prevent its volatilization during the samples preparation process. Firstly stoichiometric amounts of the staring materials tetrabuty titanate $[Ti(OC_4H_9)_4]$, bismuth nitrate pentahydrate $[Bi(NO_3)_3 \cdot 5H_2O]$, and iron nitrate nonahydrat $[Fe(NO_3)_3 \cdot 9H_2O]$ were dissolved in dilute nitric acid, and then EDTA (ethylene diamine tetraacetic acid) $[C_{10}H_{16}N_2O_8]$ and citric acid $[C_6H_8O_7 \cdot H_2O]$ were added to form a stable colloidal solution. Secondly, barium nitrate $[Ba(NO_3)_2]$ dissolved in deionized water and then acetic acid $[CH_3COOH]$ and ammonia were added. Thirdly, the barium nitrate solution was slowly dropped to the previous solution, and then ammonia was added into the solution to adjust pH to 6–7 and the mixture was stirred until transparent precursor sol was obtained. After dried, the xerogel was burned at 420 °C for 4 h. The obtained powders were grounded, and then pressed into pellets with 13 mm in diameter and 1.0 mm in thickness. For the FC sample, the pellet was sintered at 960 °C for 3 h in air and then the furnace was cooled slowly to room temperature. Whereas the water-quenched (WQ) sample was prepared by quenching the pellet into water after sintering at 960 °C for 3 h. The crystal structure was measured with an X-ray diffractometer (XRD) using Cu K_α radiation ($15° \leq 2\theta \leq 70°$) at room temperature. The microstructure was observed with a field-emission scanning electron microscope (FE-SEM, SU 8020, Hitachi). All samples were polished to 100 micron to perform the ferroelectric measurements. The bottom surface of the sintered ceramic was coated via ion sputtering with Au and then coated again with silver paste as bottom electrode. The top surface of the sintered ceramic was poked small points with silver paste, which linked Au wires as top electrode to form metal-insulator-metal capacitors. At last, the capacitors were dried at 120 °C for 10 min. The ferroelectric properties were investigated using a Sawyer–Tower circuit attached to a computer-controlled standardized ferroelectric test system (Radiant Technology 609 B). The temperature dependent dielectric constant and complex-impedance were measured with a precision LCR meter (TH2828/A/S).

3 Results and discussion

3.1 Structural and micro structural studies

The room-temperature XRD patterns of the FC and WQ samples are shown in Fig. 1. The results indicate that the two samples are pure phase with no detectable impurity phases. It was reported that $(1 − x)BiFeO_3$–$xBaTiO_3$ ceramics with $x < 0.33$ could be indexed with a rhombohedral lattice, and a morphotropic phase boundary (MPB) consisting of rhombohedral and tetragonal phases existed at a critical point of $x = 0.33$ [18]. We refined the structural parameters of the FC and WQ samples with two-phases (R3c and P4mm) model by using RIETICA software, as shown in Fig. 1a–b. It can be seen that the fits between the experimental and calculated XRD patterns are relatively good based on the consideration of the lower R_P values of 3.67 and 3.14% for the FC and WQ samples, respectively. The fitting results show that the structures of the FC and WQ samples consist of rhombohedral and tetragonal phases, which is consistent with the previous report [18]. The obtained lattice parameters a, c and unit cell volume V are $a_{R3c} = 5.631$ (2) Å, $c_{R3c} = 13.823$ (4) Å, $a_{P4mm} = 3.993$ (6) Å, $c_{P4mm} = 4.018$ (0) Å and $V_{R3c+P4mm} = 502.36$ (5) Å^3 for the FC sample, and $a_{R3c} = 5.643$ (5) Å, $c_{R3c} = 13.827$ (3) Å, $a_{P4mm} = 4.002$ (1) Å, $c_{p4mm} = 4.021$ (4) (5) Å and $V_{R3c+P4mm} = 504.69$ (9) Å^3 for the WQ sample. It is found that a, c and V of the FC sample are slightly smaller
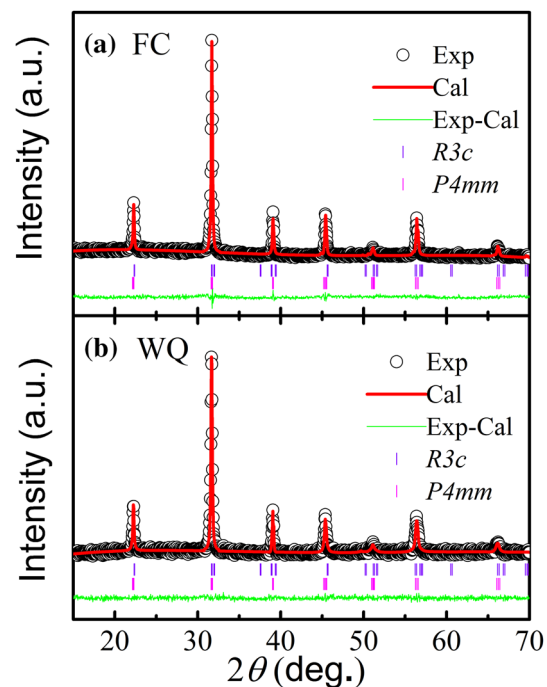

Fig. 1 XRD patterns and Rietveld refinements of 67BF–33BT solid solutions for **a** the FC sample and **b** the WQ sample

than that of the WQ sample, which may be due to the existence of more Bi vacancies in the FC sample.

Figure 2 illustrates the cross section SEM pictures of the FC and WQ samples. As shown in Fig. 2, the polyhedron particles with the typical size of 1 μm are compacted together. Both the FC and WQ samples have dense morphology with relative densities larger than 93% of the theoretical values according to measurement results by Archimedes method. The results of SEM pictures indicate that water quenching process have little effect on the microstructure of 67BF–33BT solid solution at micrometer resolution.

3.2 Ferroelectric properties

Figure 3 shows the room-temperature P–E hysteresis loops of the FC and WQ samples measured in different electric fields at 100 Hz. The P–E hysteresis loop of the FC sample with remnant polarization P_r of 16 μC/cm^2 shows a high leakage current characteristic (Fig. 3a). Whereas, the WQ sample exhibits a well-defined P–E loop with P_r of 23.1 μC/cm^2 and coercive field of 46 kV/cm in the applied electric field of 140 kV/cm (Fig. 3b). The displacement currents vs. voltage were measured to verify the ferroelectric responses of the FC and WQ samples. It can be seen that the maximum current peak near the coercive field is very feeble in the FC sample, which suggests that the polarization of the FC sample does not contribute from the domain switching but from the other factors such as leakage current or linear capacitor [23]. For the WQ sample, there is an obvious maximum current peak corresponding to the coercivity of 46 kV/cm in the P–E hysteresis loop, which confirms the occurrence of ferroelectric switching. To eliminate the contribution of nonswitchable components to the P–E hysteresis loop of the WQ sample, we performed a positive-up negative-down (PUND) measurement as shown in the inset of Fig. 3b. The polarization value obtained from the PUND measurement is close to $2P_r$ obtained from the P–E loops, implying that the
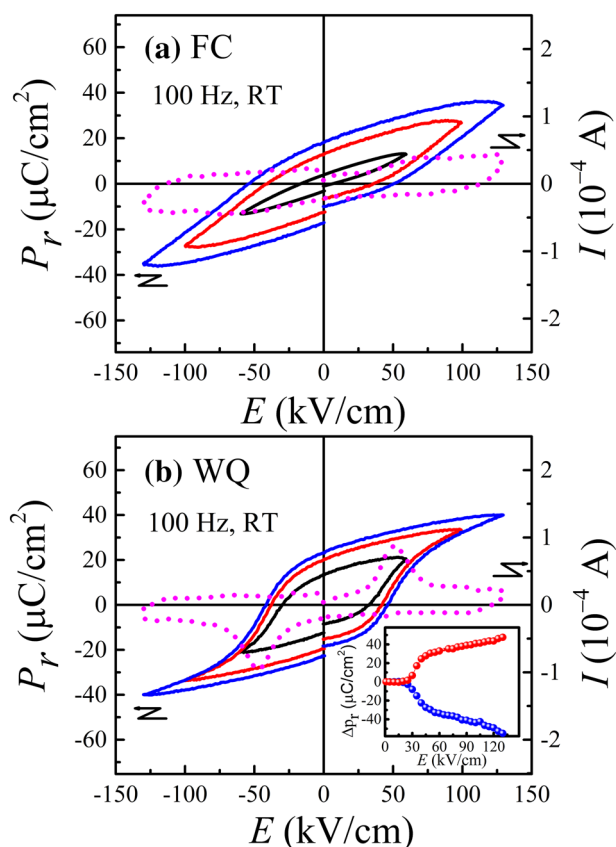

Fig. 3 P–E hysteresis loops of **a** the FC and **b** the WQ samples measured at 100 Hz at room temperature. The inset of **b** is the plot of switched polarization vs. pulse amplitude for the WQ sample from a PUND measurement

contribution of the leakage current to the remnant polarization for the WQ sample can be ruled out.

It is known that the defects including charged defects, oxygen vacancies or Bi vacancies are homogenous distributed in high temperature [19]. During the furnace cooling
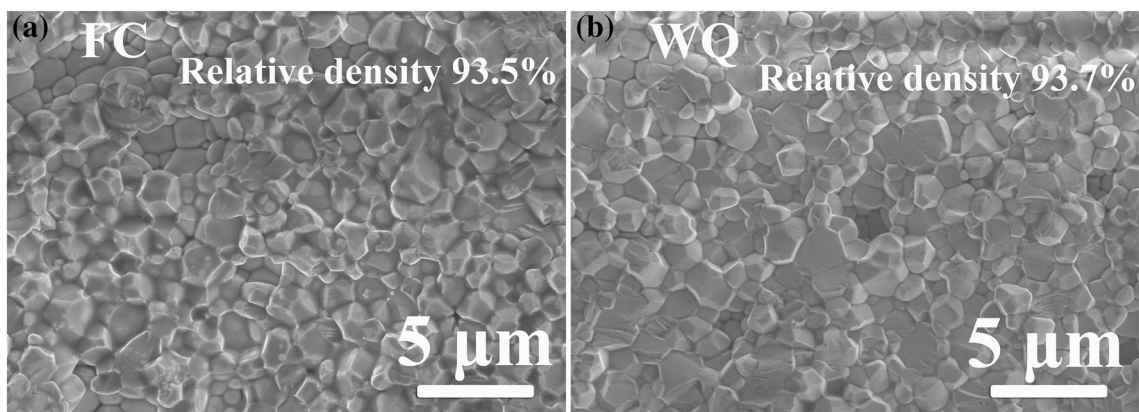

Fig. 2 SEM pictures of **a** the FC and **b** the WQ samples

process, the defects are redistributed in the low energy regions such as grain and/or domain walls, and the positively charged oxygen vacancies may bind to the negatively charged Bi defects, to form the defect dipoles, resulting in the stabilization of the domain structures and the pinning of domain walls [24, 25]. For the FC sample, the *P–E* loop is pinched and there is no obvious displacement current peak, which may be related to the pinned domain walls by the charged defects. However, for the WQ sample, the homogenous distributed defects states can be remained when the temperature rapidly goes down to RT, which may release the domain walls and obtain well-defined *P–E* loops.

Besides the RT ferroelectric performance, the thermal stability of ferroelectric material is also very important when they are used in the memory devices. So it is worth to investigate the ferroelectricity of the 67BF–33BT solid solution above room temperature. Figure 4 shows the *P–E* hysteresis loops of the FC and WQ samples measured at RT, 50 and 100 °C. For the FC sample, P_r values slightly increases with increasing temperature and reaches 22 μC/cm^2 at 100 °C, while the *P–E* loops show the characteristic of leakage current. For the WQ sample, all the *P–E* loops show a typical ferroelectric shape, and the values of remnant polarization P_r increase with increasing temperature. The ferroelectric domains are more easily to switch at high temperatures,
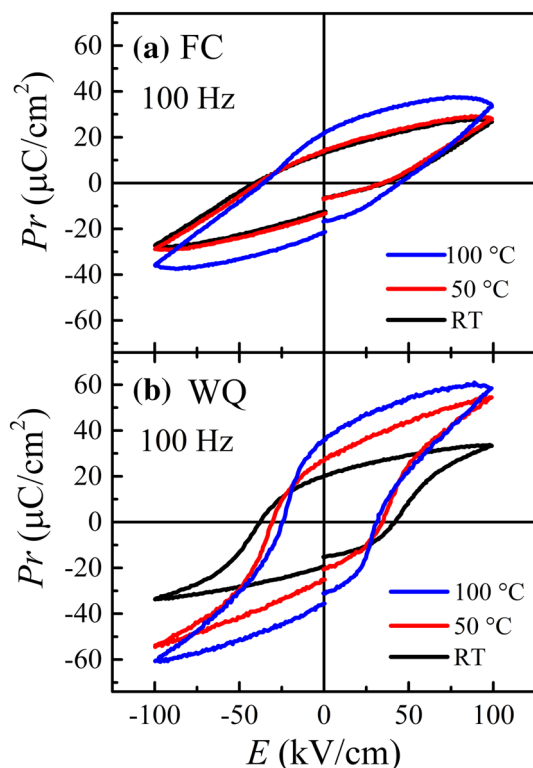
which results in the increase of P_r values and decrease of coercive fields. The enhanced polarization with increasing temperature may also be associated with the increase in the amounts of switchable domains.
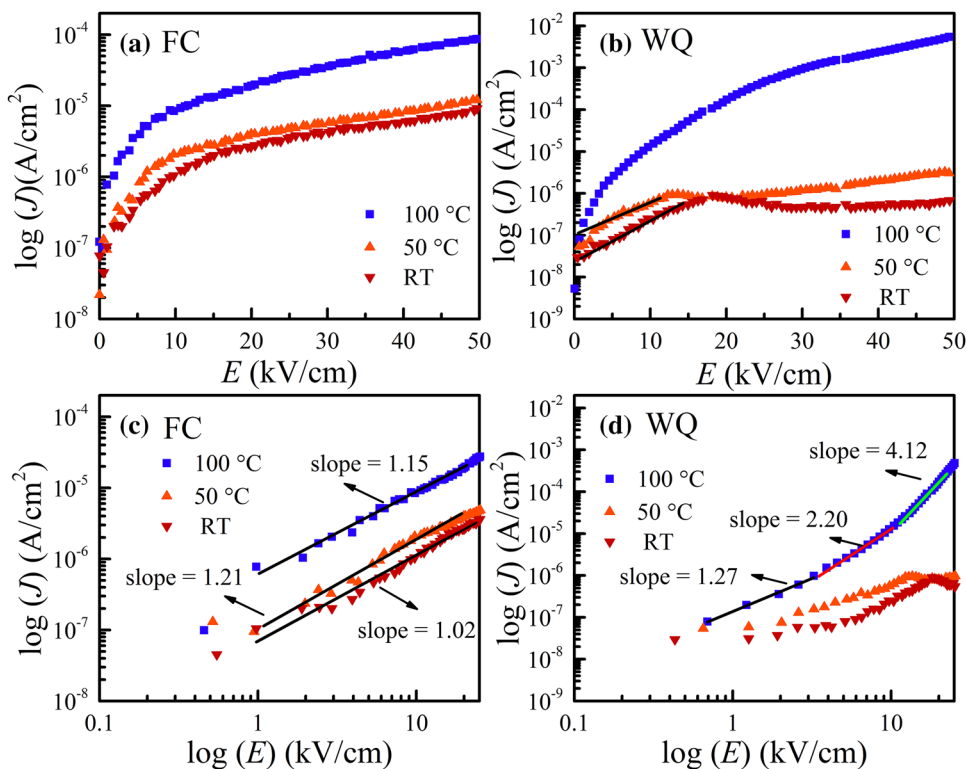
3.3 Leakage mechanisms

To study the leakage mechanisms of the FC and WQ samples, we measured the *I–V* curves for the both samples, as shown in Fig. 5. Figure 5a–b are log(*J*)– *E* curves of the FC and WQ samples. The leakage current density was recorded at RT, 50 and 100 °C. For the FC sample, the leakage current density rapidly increases with the increase in electric fields when the electric field is below 10 kV/cm, and the leakage current density also increases with the temperatures. The leakage current density of the FC sample is around 8×10^{-5} A/cm^2 under the electric field of 50 kV/cm at RT, which is one order of magnitude larger than that of the WQ sample (6.7×10^{-6} A/cm^2). The high leakage current density of the FC sample at RT is related to the existence of more Bi vacancies and oxygen vacancies compared with those of the WQ sample [18]. For the WQ sample, the RT leakage current density increases linearly with the increase of electric field below 18 kV/cm. With the temperature increasing to 50 °C, the leakage current slightly increases and the linear region moves to lower electric field of 13 kV/cm. With further increasing temperature to 100 °C, the leakage current density dramatically increases and there is no linear region in low electric fields implying that the leakage mechanisms may change.

The log(*J*) *vs.* *E* curves of the WQ sample at RT and 50 °C at low electric fields exhibit a linear behavior, i.e., log(*J*) ∝ *E*, indicating that the conduction process may be predominated by field-assisted ionic conduction [26]. Oxygen and iron ions are usually not mobile at room temperature. The field-assisted ionic conduction may occur by transfer of electrons between the neighboring Fe^{2+} and Fe^{3+} ions in a high electric field, and in such a way the Fe^{2+} ions are virtually hopping forward against the applied electric field [27]. Whereas log(*J*) *vs.* *E* curves at low electric fields of the FC sample and 100 °C of the WQ sample do not show the linear behavior implying that other conduction mechanisms may be dominant.

Ohmic conduction and the space-charge-limited conduction (SCLC) mechanisms are commonly involved in the transport behavior of $BiFeO_3$ ceramics [28–30]. Logarithmic plot of the current density and electric field is a useful tool to find the conduction mechanism involved in leakage behavior of the samples. The curves of log (*J*) *vs.* log (*E*) are plotted for the FC and WQ samples, as shown in Fig. 5c–d. For the FC sample, log (*J*) *vs.* log (*E*) curves follow a nearly linear behavior with slopes of 1.02, 1.15, 1.21 at RT, 50 and 100 °C, respectively. The linear behavior manifests that

Fig. 4 *P–E* hysteresis loops of **a** the FC and **b** the WQ samples measured at 100 Hz at RT, 50, and 100 °C

Fig. 5 log(*J*) vs. *E* plots of **a** the FC and **b** the WQ samples. Log(*J*) *vs.* log(*E*) plots of **c** the FC, **d** the WQ samples. The lines are the fitted data

an Ohmic conduction is dominant for the FC samples. The Ohmic conduction normally appears when bulk charge density is larger than the density of injected charges from the electrode.

As for the leakage current mechanism of the WQ sample at 100 °C, A power-law relationship log(*J*) *vs.* log(*E*) is used to fit the curves, as shown in Fig. 5d. The curve at 100 °C can be well fitted by three straight lines. The slope at low fields is close to one indicating a linear Ohmic conduction. With increasing the electric field, electrons will be injected into the insulator, and when the density of free electrons become greater than that of thermally stimulated free electrons, the slope is about 2, which is in good agreement with SCLC mechanism. The SCLC is expressed as [31]:

$$J_{SCLC} = 9/8\varepsilon_r\varepsilon_0\mu\theta V^2/d^3$$

where *V* is the applied voltage, ε_r is the static dielectric constant, ε_0 is the permittivity of free space, *d* is the thickness of thin film, and θ is the ratio of the total density of free electrons to the trapped electrons. With further increasing the electric filed, the leakage current increases dramatically with the slope of 4.12, which can be understood by the trap-filled-limit (TFL) law [31].

3.4 Impedance spectroscopy analysis

The complex impedance spectra Z′ *vs.* Z″ (cole–cole plot) measured at RT, 100 and 150 °C are shown in Fig. 6a–b.

As shown in the inset of Fig. 6a, the impedance spectra of both samples exhibit the straight lines indicating the insulating behavior at RT. With the temperature increasing, the tendency of formation of semicircular arcs can be seen. The radii of semicircles decrease with the increase of temperature implying an increase in conductivity. The centers of these semicircles lie on a line below the real axis indicating that the FC and WQ samples follow the non-ideal Debye behavior [9, 32]. The experimental impedance data has been analyzed with suitable equivalent circuit using the ZSimpWin software. The equivalent circuit for the FC and WQ samples can be expressed as two Resistor-CPE (R-CPE) elements parallel circuits connected in series [33] as pointed out in the inset of Fig. 6b. The R_g and R_{gb} are the resistances of the grain and grain boundary, and the fractal capacitance CPE_g and CPE_{gb} are the capacitances of grain and grain boundary, respectively. The values obtained from the fitting curves are shown in Table 1. It is found that the R_g and R_{gb}

Table 1 The R_g, R_{gb} and CPE_g, CPE_{gb} values obtained from cole–cole plot fitting

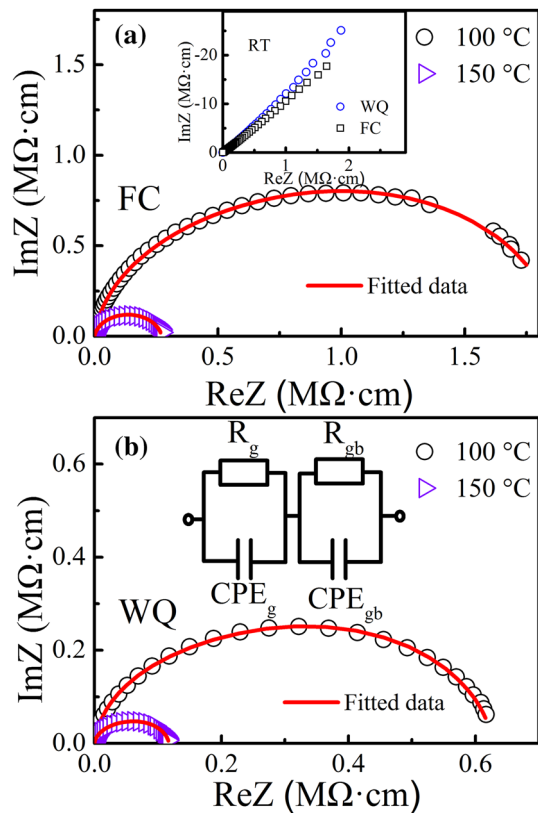| T (°C)	Samples	R_g (MΩ)	CPE_g (nF)	R_{gb} (MΩ)	CPE_{gb} (nF)
100	FC	1.094	2.183	0.771	1.999
	WQ	0.174	0.325	0.453	0.534
150	FC	0.098	7.613	0.184	4.367
	WQ	0.032	0.662	0.048	0.408

Fig. 6 Cole–Cole plots of complex-impedance ($Z = ReZ + iImZ$) of the FC and WQ samples at RT, 100 and 150 °C in the frequencies range of 100 Hz to 1 MHz. The symbols are the experimental data and the solid curves are the fitting results. The inset of **a** shows the complex-impedance measured at RT. The inset of **b** shows the equivalent circuit model

of the FC and WQ samples decrease with the increase of temperature.

3.5 Dielectric properties

Figure 7 shows the temperature dependence of dielectric constant ε_r of the FC and WQ samples at different frequencies from RT to 700 °C. The dielectric curves of the FC and WQ samples have a sharp dielectric peak, which correspond to their ferroelectric transition temperature T_c. Whereas the dielectric constant ε_r of the FC sample is smaller than that of the WQ sample. The T_c (about 457 °C) of the FC sample slightly shifts toward lower temperature compared to the WQ sample ($T_c = 470$ °C) which imply that the stability of ferroelectric state of the FC sample is weaker than that of the WQ sample. As for the FC sample, the Bi vacancies lead to the increase of disorder degree in perovskite structure, which result in the decrease of T_C [34]. The results of analysis manifest that the WQ sample may exhibit better ferroelectric properties compared with the FC sample, which is in good agreement with the measured results of P–E loops.
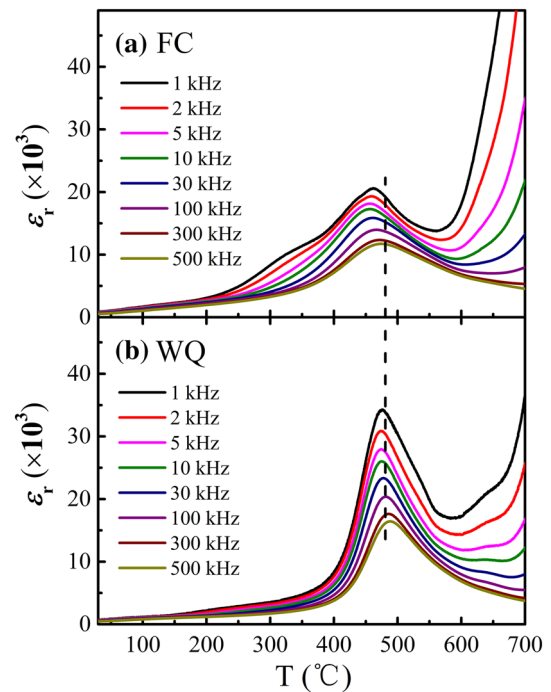

Fig. 7 Temperature dependence of dielectric constant ε_r for **a** the FC sample and **b** the WQ sample

4 Conclusion

In summary, we prepared $0.67BiFeO_3$–$0.33BaTiO_3$ solid solutions by a Pechini method followed by a quenching process and studied the structural, ferroelectric, dielectric properties and leakage mechanisms of the samples. The results of XRD Rietveld refinements show that the structures of the FC and WQ samples are consist of rhombohedral and tetragonal phases. The quenched sample exhibits well-defined P–E hysteresis loop due to the released domain walls by quenching process. The leakage mechanism of the FC sample obeys Ohmic conduction mechanism. The leakage mechanism of the WQ sample at RT and 50 °C at low electric fields is predominant by field-assisted ionic conduction, whereas the mechanisms at 100 °C can be understood by Ohmic, space charge limited, and trap-filled-limit conduction at low, moderate, and high electric fields, respectively.

References

1. J.R. Teague, R. Gerson, W.J. James, Dielectric hysteresis in single crystal BiFeO$_3$. Solid State Commun. **8**, 1073 (1970)

2. I. Sosnowskat, T. Peterlin-Neumaier, E. Steichele, Spiral magnetic ordering in bismuth ferrite. J. Phys. C: Solid State Phys. **15**, 4835–4846 (1982)

3. J. Wang, J.B. Neaton, H. Zheng, V. Nagarajan, S.B. Ogale, B. Liu, D. Viehland, V. Vaithyanathan, D.G. Schlom, U.V. Waghmare, N.A. Spaldin, K.M. Rabe, M. Wuttig, R. Ramesh, Epitaxial $BiFeO_3$ multiferroic thin film heterostructures. Science **14**, 1719–1722 (2003)

4. P. Fischer, M. PoIomska, I. Sosnowska, M. Szymanski, Temperature dependence of the crystal and magnetic structures of $BiFeO_3$. J. Phys. C: Solid State Phys. **13**, 1931–1940 (1980)

5. M. Valant, A.-K. Axelsson, N. Alford, Peculiarities of a solid-state synthesis of multiferroic polycrystalline $BiFeO_3$. Chem. Mater. **19**, 5431–5436 (2007)

6. S.M. Selbach, M.-A. Einarsrud, T. Grande, On the thermodynamic stability of $BiFeO_3$. Chem. Mater. **21**, 169–173 (2009)

7. T. Rojac, M. Kosec, B. Budic, N. Setter, D. Damjanovic, Strong ferroelectric domain-wall pinning in $BiFeO_3$ ceramics. J. Appl. Phys. **108**, 074107 (2010)

8. G. Catalan, J.F. Scott, Physics and applications of bismuth ferrite. Adv. Mater. **21**, 2463–2485 (2009)

9. M.M. Kumar, A. Srinivas, S.V. Suryanarayana, Structure property relations in $BiFeO_3$/$BaTiO_3$ solid solutions. J. Appl. Phys. **87**, 855 (2000)

10. T. Kanai, S. Ohkoshi, A. Nakajima, T. Watanabe, K. Hashimoto, A ferroelectric ferromagnetcomposed of $(PLZT)_{(x)}$-$(BiFeO_3)_{(1-x)}$ solid solution. Adv. Mater. **13**, 487–490 (2001)

11. W.J. Huang, J. Yang, Y.F. Qin, P. Xiong, D. Wang, L.H. Yin, X.W. Tang, W.H. Song, P. Tong, X.B. Zhu, Y.P. Sun, Room temperature multiferrocity and magnetodielectric properties of ternary $(1–x)$ $(0.94Bi_{0.5}Na_{0.5}TiO_3$-$0.06BaTiO_3)$-$xBiFeO_3$ $(0 \leq x \leq 0.9)$ solid solutions. Appl. Phys. Lett. **111**, 112902 (2017)

12. L. Wu, B. Shen, Q.R. Hu, J. Chen, Y.P. Wang, Y.D. Xia, J. Yin, Z.G. Liu, Giant electromechanical strain response in lead-free $SrTiO_3$ doped $(Bi_{0.5}Na_{0.5}TiO_3$-$BaTiO_3)$-$LiNbO_3$ piezoelectric ceramics. J. Am. Ceram. Soc. **100**, 4670–4679 (2017)

13. X. Liu, F. Li, P. Li, J.W. Zhai, B. Shen, B.H. Liu, Tuning the ferroelectric-relaxor transition temperature in NBT-based lead-free ceramics by Bi nonstoichiometry. J. Eur. Ceram. Soc. **37**, 4585–4595 (2017)

14. S.O. Leontsev, R.E. Eitel, Dielectric and piezoelectric properties in Mn-modified $(1-x)BiFeO_3$-$xBaTiO_3$ ceramics. J. Am. Ceram. Soc. **92**, 2957–2961 (2009)

15. H.B. Yang, C.R. Zhou, X.Y. Liu, Q. Zhou, G.H. Chen, W.H. Li, H. Wang, Piezoelectric properties and temperature stabilities of Mn- and Cu-modified $BiFeO_3$-$BaTiO_3$ high temperature ceramics. J. Eur. Ceram. Soc. **33**, 1177–1183 (2013)

16. Y.X. Wei, X.T. Wang, J.T. Zhu, X.L. Wang, J.J. Jia, Dielectric, ferroelectric, and piezoelectric properties of $BiFeO_3$-$BaTiO_3$ ceramics. J. Am. Ceram. Soc. **96**, 3163–3168 (2013)

17. J. Chen, J.L. Wang, H.Y. Dai, T. li, Z.P. Chen, Investigations on the structure, defects, electrical and magnetic properties of Ni-substituted $BiFeO_3$ ceramics. J. Mater. Sci.: Mater. Electron. **27**, 11151–11157 (2016)

18. M.H. Lee, D.J. Kim, J.S. Park, S.W. Kim, T.K. Song, M.-H. Kim, W.-J. Kim, D. Do, Il-K. Jeong, High-performance lead-free piezoceramics with high curie temperatures. Adv. Mater. **27**, 6976–6982 (2015)

19. S. Kim, G.P. Khanal, S. Ueno, C. Moriyoshi, Y. Kuroiwa, S. Wada, Revealing the role of heat treatment in enhancement of electrical properties of lead-free piezoelectric ceramics. J. Appl. Phys. **122**, 014103 (2017)

20. D.S. Kim, C. Cheon, S.S. Lee, J.S. Kim, Effect of cooling rate on phase transitions and ferroelectric properties in $0.75BiFeO_3$-$0.25BaTiO_3$ ceramics. Appl. Phys. Lett. **109**, 202902 (2016)

21. G.L. Yuan, S. Wing, Enhanced piezoelectric and pyroelectric effects in single-phase multiferroic $Bi_{1-x}Nd_xFeO_3$ $(x = 0-0.15)$ ceramics. Appl. Phys. Lett. **88**, 062905 (2006)

22. X. Liu, B.H. Liu, F. Li, P. Li, J.W. Zhai, B. Shen, Relaxor phase evolution and temperature-insensitive large strain in B-site complex ions modified NBT-based lead-free ceramics. J. Mater. Sci. **53**, 309–322 (2018)

23. L. Jin, F. Li, S.J. Zhang, Decoding the fingerprint of ferroelectric loops: comprehension of the material properties and structures. J. Am. Ceram. Soc. **97**, 1–27 (2014)

24. U. Robels, G. Arlt, Domain wall clamping in ferroelectrics by orientation of defects. J. Appl. Phys. **73**, 3454 (1993)

25. M. Hagiwara, S. Fujihara, Effects of CuO addition on electrical properties of $0.6BiFeO_3$-$0.4(Bi_{0.5}K_{0.5})TiO_3$ lead-free piezoelectric ceramics. J. Am. Ceram. Soc. **98**, 469–475 (2015)

26. P.J. Harrop, *Dielectrics*. (Butterworths, London, 1972)

27. X.D. Qi, J. Dho, R. Tomov, M.G. Blamire, J.L. MacManus-Driscoll, Greatly reduced leakage current and conduction mechanism in aliovalent-ion-doped $BiFeO_3$. Appl. Phys. Lett. **86**, 062903 (2005)

28. S.J. Chu a, M. Zhang, H.L. Deng, Z.H. Wang, Y. Wang, Y.H. Pan, H. Yan, Investigation of doping effect on electrical leakage behavior of $BiFeO_3$ ceramics. J. Alloy. Compd. **689**, 475–480 (2016)

29. A.R. Makhdoom, M.J. Akhtar, M.A. Rafiq, M.M. Hassan, Investigation of transport behavior in Ba doped $BiFeO_3$. Ceram Int. **38**, 3829–3834 (2012)

30. J. Wei, Y. Liu, X.F. Bai, C. Li, Y.L. Liu, Z. Xu, P. Gemeiner, R. Haumont, I.C. Infante, B. Dkhil, Crystal structure, leakage conduction mechanism evolution and enhanced multiferroic properties in Y-doped $BiFeO_3$ ceramics. Ceram Int. **42**, 13395–13403 (2016)

31. C. Wang, M. Takahashi, H. Fujino, X. Zhao, E. Kume, T. Horiuchi, S. Sakai, Leakage current of multiferroic $(Bi_{0.6}Tb_{0.3}La_{0.1})$ FeO_3 thin films grown at various oxygen pressures by pulsed laser deposition and annealing effect. J. Appl. Phys. **99**, 054104 (2006)

32. N. Dhifallah, B. Hehlen, M. Dammak, H. Khemakhem, Phase formation and dielectric study of Bi doped $(Ba_{0.8}Sr_{0.2})$ $Ti_{0.95}(Zn_{1/3}Nb_{2/3})_{0.05}O_3$ ceramic. Mater. Chem. Phys. **181**, 176–186 (2016)

33. N. Kumar, A. Shukla, R.N.P. Choudhary, Structural, electrical and magnetic characteristics of Ni/Ti modified $BiFeO_3$ lead free multiferroic material. J. Mater. Sci.: Mater. Electron. **28**, 6673–6684 (2017)

34. T. Zheng, Y. Ding, J.G. Wu, Bi nonstoichiometry and composition engineering in $(1-x)Bi_{1+y}FeO_{3+3y/2}$-$xBaTiO_3$ ceramics. RSC Adv. **6**, 90831 (2016)